Near-Perfect Space-Wave to Surface-Wave Coupler Enabled Conformal Space Wave Transporting Metasurfaces

Jordan Budhu, *Member, IEEE*

***Abstract*—A technique for the design of conformal metasurfaces with two spatially disconnected space wave ports connected by a surface wave is presented. The passive and lossless metasurface absorbs the incident wave at port 1, converts it nearly perfectly into a surface wave which transports the energy along an arbitrarily shaped/curved metasurface to port 2, then reradiates the captured power as a radiated field with control over its amplitude and phase. Since the incident field is seen to disappear at the input port and reappear at a spatially dislocated port as a new formed beam, the space wave can be said to have been seamlessly transported from one point in space to another. The metasurface consists of a single, conformal, spatially variant, impedance sheet supported by a conformal grounded dielectric substrate of the same shape. It is modeled using integral equations. The integral equations are solved using the method of moments (MoM). The impedances of the sheet are optimized using the adjoint variable method to achieve the near perfect wave transportation operation from a passive and lossless metasurface. MATLAB codes and COMSOL Multiphysics simulation files for all designs presented in this paper are available for download as supplemental material files. Possible applications include channel optimization for cellular networks, inexpensive power harvesting, sensing, around-the-corner radar, and cloaking.**

***Index Terms*—Conformal, Metasurface, Plane wave coupler, integral equations, method of moments, adjoint variable optimization**

I. Introduction

THE design of metasurfaces to create tunnel-like connections through space (with a finite travel time from port to port) connecting two space wave ports at distant locations is addressed in this paper (see Fig. 1). The incident space wave field is absorbed at port 1, perfectly converted into a surface wave which connects the two ports and transfers power between them, and reradiated from port 2 located at a distant location. The reradiated field from port 2 is designed with arbitrary control over its phase *and* amplitude in a completely passive and lossless way utilizing nearly all (over 97.5%) of the power contained in the incident field over port 1. As the metasurface transfers nearly all of the available power in the incident wave to the reradiated wave, the operation is said to be near perfect.

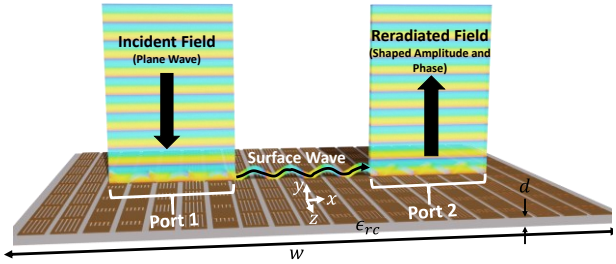

Fig. 1. Transporting metasurface geometry. Note, the unit cells are shown enlarged for clarity. The actual metasurface contains 200 unit cells each $\lambda_0/20$ wide.

The enabling technology for the presented designs is near perfect space-wave to surface-wave couplers. Although these devices have been demonstrated before for planar [1]–[4] and cylindrical surfaces [5]–[7], near perfect coupling over an arbitrarily shaped non-canonical conformal surface has not been shown. Furthermore, complex-valued field control over non-canonical conformal surfaces using passive and lossless metasurfaces has also not been shown. In this paper, near perfect space-wave to surface-wave couplers enable wave transportation of incident beams to spatially dislocated ports along any desired shape surface and with complex-valued field control of the reradiated beam from a completely passive and lossless metasurface.

The metasurface itself is a textured interface, modeled as a spatially variant homogenized purely reactive impedance sheet supported by a grounded dielectric substrate [8]. The metasurface is capable of complex-valued radiated field control and seamless conversion between guided and unguided modes in a lossless or perfect manner. It is modeled using integral equations [9]–[11], the integral equations are solved using the method of moments technique [12], and the reactances of the impedance sheet optimized using the adjoint variable method [11], [13], [14]. For an overview of the design procedure, see [11], [15]. A customized integral equation for the design of the conformal cases specific to this paper can be found in the appendix of this paper. The metasurface can be made to conform to any shape such as the corner of a building (see Fig. 10 for preview) or a general non-canonical curvilinear surface (see Fig. 15 for preview) for example. We will first present a planar design to demonstrate the near perfect wave transportation function and understand its operation.

Jordan Budhu is with Virginia Tech, Blacksburg, VA 24060 USA. (e-mail: jbudhu@vt.edu).

Color versions of one or more of the figures in this article are available online at http://ieeexplore.ieee.org

Subsequently, the same functionality from conformal geometries will be shown.

Similar planar transporting metasurfaces have appeared in recent scientific works. In [2], a planar wave transporting metasurface was designed by juxtaposing three separate metasurfaces, two space wave to surface wave couplers separated by a metasurface supporting a pure surface wave. The overall metasurface system laterally shifts a plane wave incident at an angle of 30° on the left-hand side of the metasurface to a transmitted wave emanating from the right-hand side of the metasurface at an angle of $-7.2°$ with respect to the normal. Due to the analytical design procedure, the metasurface junctions scatter and reduce the efficiency. Also, the coupling metasurfaces do not perfectly convert the incident fields to surface wave fields. The authors report an efficiency of only 10%, and hence the wave transportation cannot be deemed perfect. Furthermore, the approach cannot control both the phase and amplitude of the transmitted field and hence does not have the capability of complex-valued field control. The metasurfaces in the referenced work are also not conformal.

In [16], a planar teleporting metasurface is designed using the principles of $\mathcal{PT}$ symmetry. A reactive layer is sandwiched between an absorbing lossy Salisbury screen layer matched to free space and an active layer with a negative impedance also matched to free space. An incident plane wave is absorbed nearly completely by the lossy layer, while the inductive perforated layer allows the remaining small amount of power to couple to the active layer where it is resonantly amplified to recreate or teleport the incident plane wave to the opposite side. Although this device requires active and lossy components, the loss and gain are balanced according to $\mathcal{PT}$ symmetry and hence represents an overall lossless system. Nonetheless, the structure is planar, requires active layers which complicates fabrication and cannot achieve beamforming.

This paper is organized as follows. In section II, we present a planar example. Next, in section III, two conformal examples will be presented. The first contains planar coupling regions and a conformal surface wave region. The second contains both conformal coupling regions and conformal surface wave regions. Some concluding remarks are provided in section IV. An $e^{j\omega t}$ time convention is assumed and suppressed throughout the paper.

II. Wave Transporting Metasurface Design and Analysis

We first present a planar wave transporting metasurface to understand the wave transportation function as it pertains to metasurfaces. The metasurface geometry is shown in Fig. 1. The electromagnetics problem is 2-dimensional (out-of-plane wavenumber is zero) and hence the geometry is invariant in the z-direction. The patterned metallic cladding, described by a spatially variant homogenized sheet impedance $\eta_s(x)$, is supported by a grounded dielectric substrate of thickness $d = 1.27$mm (50mil) and complex relative permittivity $\epsilon_{rc} = \epsilon_r(1 - jtan\delta) = 2.2 - j0.002$. The impedance sheet is broken into 200 unit cells of width $\lambda_0/20$ each at $f = 10$GHz. The metasurface is therefore $w = 200(\lambda_0/20) = 10\lambda_0$ wide along the x-axis. The design of the transporting metasurface begins

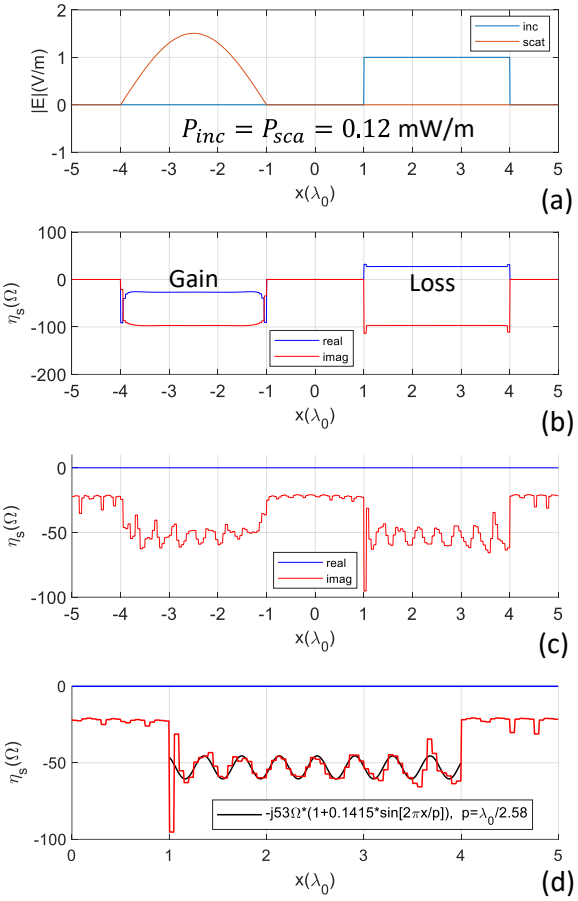

Fig. 2. (a) Specification of incident and scattered field amplitudes at the metasurface plane. NOTE: the input/output ports have been swapped with respect to Fig. 1. Metasurface sheet impedances of (b) Initial local active/lossy metasurface design and (c) Subsequent non-local passive and lossless design. (d) Zoomed in view within the input port region of the non-local passive and lossless design shown superimposed with the sheet impedance modulation function $\eta_s = -j53\Omega\left[1 + 0.1415\sin\left(\frac{2\pi x}{p}\right)\right]$ where $p = \lambda_0/2.58$.

by specifying the desired total field tangential to the metasurface. The incident field is assumed a normally incident plane wave illuminating only the right-hand portion of the metasurface between $\lambda_0 \le x \le 4\lambda_0$ as shown in Fig. 2a. The reradiated (scattered) field is defined to have both a cosine tapered amplitude and uniform phase (complex-valued field control) exiting from only the left-hand portion between $-4\lambda_0 \le x \le -\lambda_0$. Critically, the absolute level of the amplitude in V/m of the scattered field is chosen to conserve power globally meaning the total power in the incident field, $P_{inc} = |E_0|^2/2\eta_0 = 0.12$ mW/m for a unit strength plane wave, is equal to the total power in the scattered field. This definition will lead to the near perfect transportation, i.e., all the power is transferred from the incident field to the scattered field.

A. Local Active/Lossy Design

The metasurface design algorithm [11] starts from a local active/lossy (Ac/Ly) design used as a seed for the non-local passive/lossless (Pa/Ll) design. The local active/lossy design is

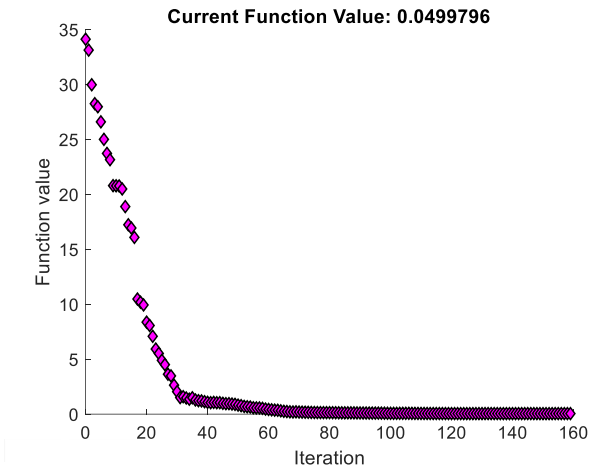

Fig. 3. Optimizer convergence plot.

obtained from the solution of the governing integral equations given the desired total field, E^{tot}, associated with the wavefront transformation (see (16) and (17)). By solving the integral equations, the surface current density, J_s, on the metasurface is obtained, thereby allowing for the direct calculation of the metasurface impedances, η_s, following from the boundary condition $\eta_s = E^{tot}/J_s$ (see Fig. 2b). As expected, the metasurface is lossy over the incident field region, and contains gain in the scattered field region. Furthermore, the loss and gain are balanced as a result of the choice of the scattered field amplitude. A transmission line model can be used to understand the result. Modelling the panel as a transmission line terminated in a shunt impedance representing the metasurface in parallel with an inductance representing the thin grounded dielectric substrate, the sheet impedance can be calculated as

$$\eta_{s,inc} = -\frac{\eta_0\eta_d \tan\beta d\,(1+\Gamma)}{\eta_d \tan\beta d\,(\Gamma-1) - j\eta_0\,(1+\Gamma)}\bigg|_{\Gamma=0e^{j0}} = 27.54 - j98\Omega \quad (1)$$

where $\eta_{s,inc}$ is the sheet impedance within the illuminated portion of the metasurface, Γ is the reflection coefficient looking into the parallel load, β is the wavenumber in the dielectric region, and η_0 and η_d are the intrinsic impedances of the free space and dielectric regions, respectively. For perfect absorption, the reflection coefficient should be zero. The resulting sheet impedance in (1) matches the numerically obtained value in Fig. 2b. In order for power conservation, the power absorbed in the lit region must exit the output region, and hence the sheet impedance in the scattered field region can be described as $\eta_{s,sca} = -27.54 - j98\Omega$. Note, since the shape of the amplitude differs between the two port regions, the sheet impedance tapers are different at the ends of their respective regions. Thus, the desired functionality of wave transportation can be achieved with a local balanced active/lossy metasurface described by the sheet impedances in Fig. 2b. In this case, the beam would teleport as the incident energy is not transported to the output beam but rather the output beam is created through resonant amplification given some small diffractive coupling. Its balanced loss and gain operating principle is similar to the balanced loss and gain of the $\mathcal{PT}$ symmetric teleporting structure in [16]. In both cases, although the incident energy itself does not teleport, a small diffractive coupling is necessary

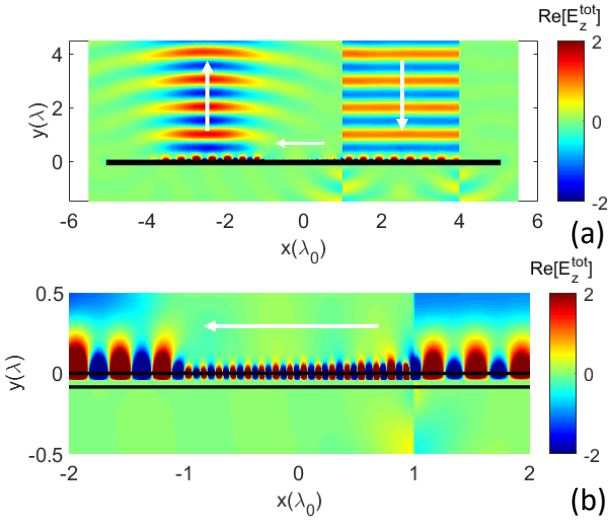

Fig. 4. (a) Real part of the total electric field. (b) Zoomed in to show surface wave connecting the input and output ports.

to excite the gain medium to resonantly create the teleported beam.

B. *Non-local Passive/Lossless Design*

A purely passive/lossless metasurface eases fabrication and avoids unnecessary complexity. To that end, the local active/lossy metasurface is used as a seed design to obtain a non-local passive/lossless design with the same performance. Since the power is balanced, a surface wave can carry the power from the lossy region to the active region. In this case, the metasurface transports the energy to the output port rather than teleports it. However, from an outside perspective, the beam is seen to disappear and reappear somewhere else in space.

The integral equation solver is coupled with an adjoint variable optimizer to obtain the non-local design [11]. To this end, the $N = 200$ reactances of the unit cells comprising the metasurface are arranged in an N-dimensional space with each reactance varying along an orthogonal axis. A surface is defined in this space as $g(x) = f(X_1, X_2, X_3, \ldots, X_N)$ and represents the response of the metasurface as a function of its reactances X_N. The cost function g is designed such that its minimum represents the optimal solution

$$g\left(\vec{X}_n\right) = \frac{1}{2}\Delta\vec{E}^{\dagger}\vec{E} \quad (2)$$

where † denotes the conjugate transpose and

$$\Delta\vec{E} = \vec{E}_{nf,Pa/Ll}\left(\vec{r}_m\right) - \vec{E}_{nf,Ac/Ly}\left(\vec{r}_m\right) \quad (3)$$

The M observation points $\vec{r}_m$ of the electric near field $\vec{E}_{nf}$ are defined along a contour the same shape and dimension as the metasurface and displaced one wavelength above it. The optimizer is seeded with the reactive part of Fig. 2b; and then the gradient of (3), defined in the appendix of [11], is used to descend along g to its minimum.

The optimizer converged to a value of $g = 0.05$ in 160 iterations (see Fig. 3). The optimal non-local metasurface sheet impedance is shown in Fig. 2c and the near fields computed from the non-local design are shown in Fig. 4. Three distinct regions are evident, a spatially modulated input and output port connected by a nearly constant surface wave region. Sharp

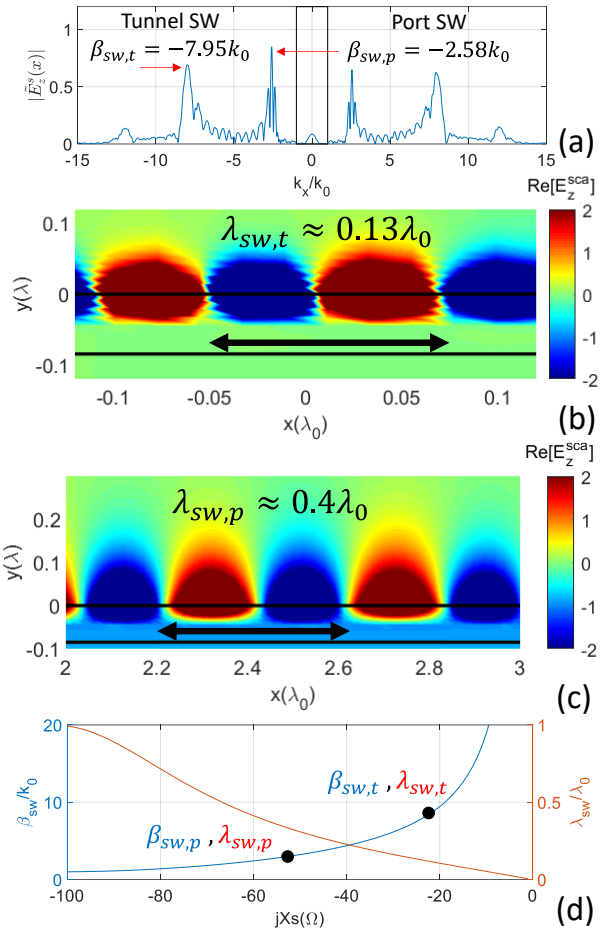

Fig. 5. (a) Amplitude spectrum of the scattered electric field at the metasurface plane. (b) Zoomed in view of Fig. 4a within the tunnel region to show tunnel surface wave wavelength. (c) Zoomed in view of Fig. 4a within the input port region to show port surface wave wavelength. (d) Dispersion curve relating the surface wavenumber and wavelength to the homogenized sheet reactance.

discontinuities in the sheet impedance of Fig. 2c excite a number of auxiliary surface waves in the input and output port regions (in addition to the prominent surface wave within the port regions and within the tunnel region connecting the two ports) responsible for redistributing power transversally within the port region facilitating passivity and losslessness [11], [17]. These perturbations also aid in obtaining a seamless transition region between the ports and the connecting surface wave region increasing the overall port-to-port power transfer efficiency.

The surface waves can be visualized in Fig. 5a. Figure 5a shows the amplitude of the plane wave spectrum of the scattered electric field evaluated on the metasurface. The tunnel surface wave responsible for transporting power between the ports is evident at $\beta_{sw,t} = -7.95k_0$. This wavenumber is in agreement with the sheet impedance of $\eta_s = -j22\Omega$ in the tunnel region in Fig. 2c since a sheet of this impedance supports a surface wave of wavenumber $\beta_{sw,t} = -7.95k_0$. This can be verified by viewing the dispersion curves plotted in Fig. 5d. In Fig. 5d, a plot of the surface wavenumber and wavelength versus the sheet reactance of the metasurface is shown. The plot is

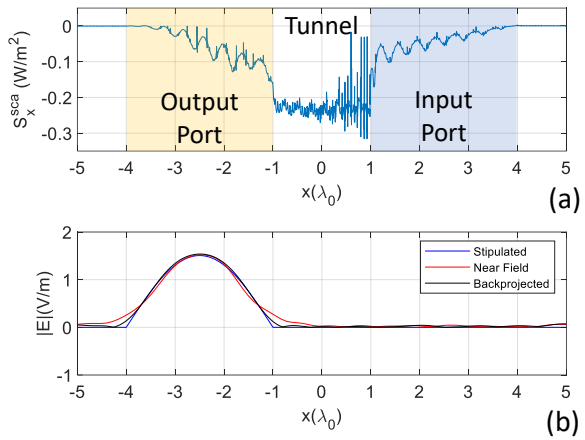

Fig. 6. (a) x-component of the Poynting vector at the plane of the metasurface. (b) Line cut of near electric scattered field amplitude at a height of one wavelength above the metasurface.

obtained using the Transverse Resonance Technique [11]. A reactive sheet impedance of $\eta_s = -j22\Omega$ is seen to support a surface wave of wavenumber $\beta_{sw,t} = -7.95k_0$. The surface wave wavelength can also be verified to agree with the curves of Fig. 5d. In Fig. 5b, a zoomed in view of the surface wave in the tunnel region is shown. The measured wavelength agrees with the dispersion curves.

The amplitude spectrum in Fig. 5a also shows another peak at $\beta_{sw,p} = -2.58k_0$, which is the surface wave generated from the incident plane wave within the input port region. Figure 5d shows this surface wavenumber is associated with a sheet impedance of $\eta_s = -j53\Omega$ in agreement with the average of the sheet impedances shown in Fig. 2c within the input port region. The sheet impedance modulation within the input port region can be understood by noting that for broadside radiation of the $n = -1$ harmonic from a surface wave of wavenumber $\beta_{sw,p} = -2.58k_0$, the period of the modulation should be $k_{xn} = \beta_{sw,p} - 2\pi/p \Rightarrow 0 = \beta_{sw,p} - 2\pi/p$ or $p = 2\pi/\beta_{sw,p} = \lambda_0/2.58$. Shown in Fig. 2d, a sinusoidal sheet impedance modulation function with this period is fit to the non-local passive/lossless metasurface sheet reactances. As can be seen, the modulation period corresponding to the $n = -1$ harmonic for broadside radiation fits the optimized sheet reactances well. The perturbations of the reactances around this analytic result excite the auxiliary surface waves and lead to the near perfect coupling. No other spatial harmonics fall within the light cone. A zoomed in view of the port surface wave within the input port region is shown in Fig. 5c. The measured surface wave wavelength is also in agreement with the dispersion curves in Fig. 5d.

Finally, a remark on the spectrum limits. The spectrum has a cut-off at $\beta_{sw} = 10k_0$ which is the highest wavenumber possible as the onset of a stop-band at $\beta_{sw} = \pi/d = 0.1k_0$ for the chosen unit cell discretization of $d = \lambda_0/20$ occurs at this wavenumber. This corresponds to a maximum sheet impedance of $-j20\Omega$ according to Fig. 5d. For this reason, hard limits of $-j20\Omega$ on the impedances during the optimization phase were set, and is why the tunnel sheet impedance is approximately $-j20\Omega$. The remaining evanescent spectrum is due to the sharp

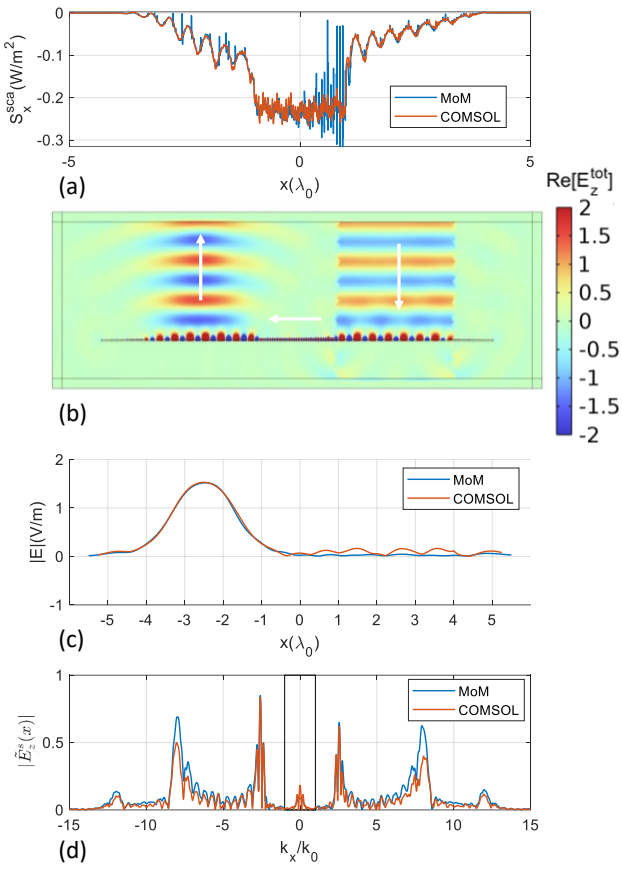

Fig. 7. COMSOL Multiphysics simulation results. (a) x-component of the Poynting vector at the plane of the metasurface. (b) Real part of the total electric field. (c) Line cut of near electric scattered field amplitude at a height of one wavelength above the metasurface. (d) Amplitude spectrum of the scattered electric field at the metasurface plane.

perturbations in the sheet impedances of Fig. 2c. These surface waves are responsible for redistributing power transversally within the port regions and at their transitions with the surface wave region in order to achieve passivity and losslessness.

The power in the surface wave can be seen to grow approximately linearly in agreement with the conclusions in [3] in Fig. 6a, although here the spectrum (Fig. 5a) contains many spatial harmonics rather than the single harmonic considered in [3] and the metasurface is strongly non-local. The figure shows the x-component of the Poynting vector, $S_x^{sca} = -(1/2)Re[E_z^{sca} H_y^{sca*}]$. H_y^{sca} was obtained by taking the inverse Fourier transform of $\tilde{E}_z^{sca} k_x/\eta_0 k_0$, where $\tilde{E}_z^{sca}$ is the electric field spectrum at the plane of the metasurface (the amplitude of $\tilde{E}_z^{sca}$ is shown in Fig. 5a). The power density in the surface wave is shown to increase from zero within the input port region approximately linearly as more of the power in the plane wave is absorbed, then become constant through the tunnel region as the power is carried to the output port region, and finally decay approximately linearly in the output port region to zero as the power is shed into the scattered beam. The oscillations in the power density profile occur due to the interference between the similarly polarized incident and surface wave fields.

Next, to show the metasurface perfectly converts the incident plane wave at port 1 to the complex-valued scattered field at

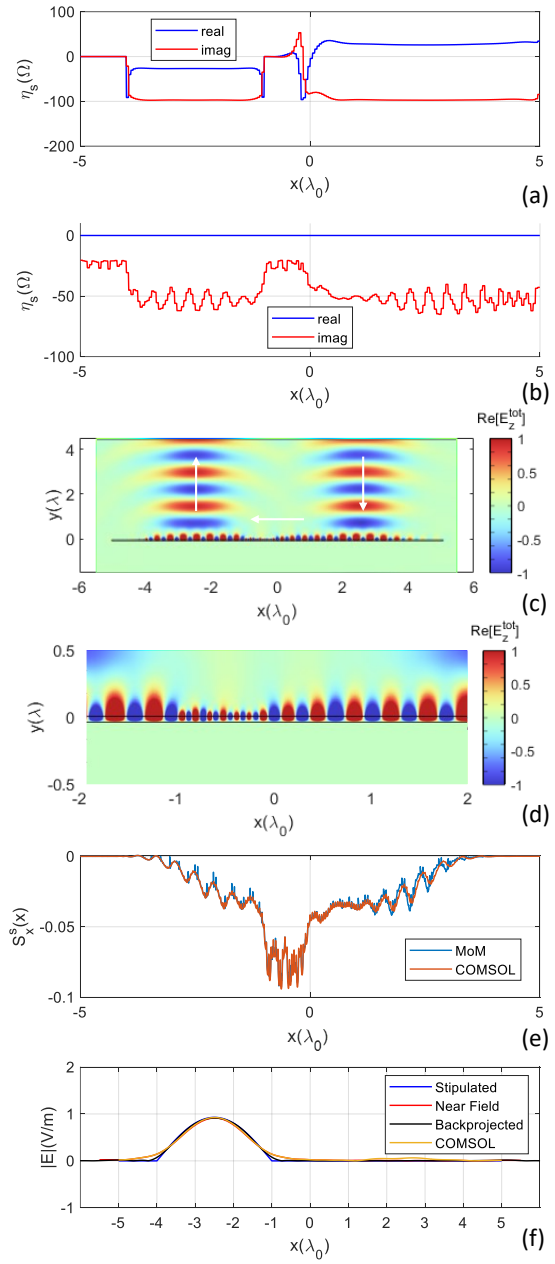

Fig. 8. Metasurface sheet impedances of (a) Initial local active/lossy metasurface design and (b) Subsequent non-local passive and lossless design. (c) Real part of the total electric field from the COMSOL Multiphysics simulation. (d) Zoomed in of (c) to show surface wave connecting the input and output ports. (e) x-component of the Poynting vector at the plane of the metasurface. (f) Line cut of near electric scattered field amplitude at a height of one wavelength above the metasurface.

port 2, the near electric field was calculated along a horizontal line one wavelength above the metasurface. In Fig. 6b, the stipulated scattered field amplitude (replicated from Fig. 2a), the directly calculated (from the induced surface currents) scattered near field amplitude, and the backprojected far fields are all shown compared. It is evident that the non-local metasurface nearly perfectly creates the stipulated near field amplitude, and hence transfers all power in the incident plane wave to the output scattered field. Integrating the power density

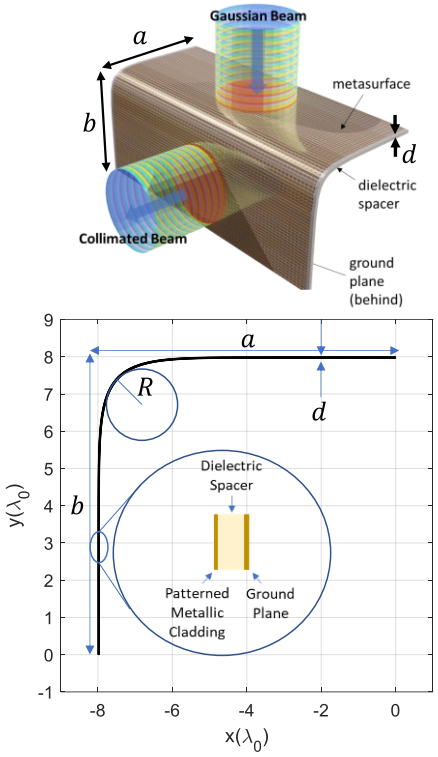

Fig. 9. Conformal transporting metasurface geometry.

along a horizontal line one wavelength above the metasurface yields $P_{sca,stip} = 0.12\text{mW/m}$ and $P_{sca,nf} = 0.1198\text{mW/m}$ giving a port-to-port transfer efficiency of 99%.

Lastly, to provide an independent verification of the transporting metasurface, the design was imported into COMSOL Multiphysics and a full-wave simulation performed. The results are compared to the MoM results in Fig. 7. As can be seen, the independent full-wave verification corroborates our results.

C. Gaussian Beam Illumination

Although it leads to intuitive results, the finite-width non-diffracting plane wave used to illuminate port 1 in the previous section is non-physical. This is evident in the shadow region behind the metasurface where the non-diffracting incident field does not totally cancel the diffracting scattered field. To model a more physical excitation, the same metasurface is illuminated with a Gaussian beam [18] with a waist radius of $w_0 = \lambda_0$ at the metasurface plane. The center of the waist is located at $x = 2.5\lambda_0$ and $y = 0$. For this example, both the MATLAB design codes and the COMSOL Multiphysics verification models are available through the IEEE DataPort at [19].

The design procedure was repeated with the Gaussian beam illumination in place of the plane wave. All other parameters were kept the same as the previous design. The resultant sheet impedances of the active/lossy design and the passive/lossless design are shown in Fig. 8a and Fig. 8b, respectively. As can be seen, the boundary of the input port is now not sharply defined, but rather spread out as the Gaussian beam illumination does not have sharp boundaries. Nonetheless, we see the same features, sinusoidal like modulation within both the input and output port regions. The real part of the total electric field for the passive/lossless design of Fig. 8b is obtained using

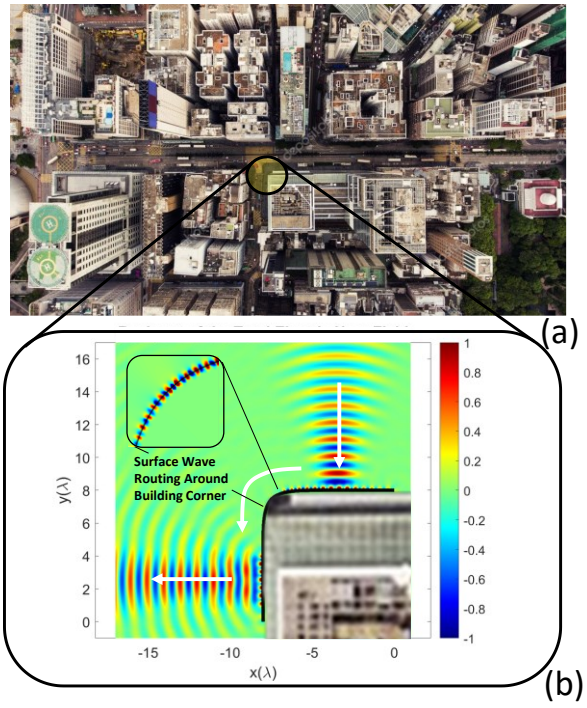

Fig. 10. (a) An urban environment. (b) Simulation results of a conformal transporting metasurface which routes plane waves around corners of buildings.

COMSOL Multiphysics and is plotted in Fig. 8c and Fig. 8d. The transverse power density (Fig. 8e) and scattered near field obtained along a line one wavelength above the metasurface (Fig. 8f) show excellent agreement with COMSOL Multiphysics. The ratio of the integrated scattered and incident field power densities produces a result of 97.5% for the port-to-port transfer efficiency.

III. Conformal Transporting Metasurfaces

By incorporating conformal geometry modelling capabilities into the integral equation/moment method algorithm (see Appendix), transporting metasurfaces connecting two distant non-colinear ports in space can be accomplished (see Fig. 9). These types of transporting metasurfaces can be useful for channel optimization in urban environments where the window-pane sized metasurface conforms to the corner of a building for example (see Fig. 10).

A. Conformal Metasurface for Communications Channel Optimization

In Fig. 9, the geometry of a conformal transporting metasurface which routes the surface wave around a 90° bend is shown. The metasurface is parameterized by a superquadric function with $p = 10$,

$$\left.\begin{aligned} x(u,v) &= \frac{v}{\sqrt[p]{\left(\frac{\cos u}{a}\right)^p + \left(\frac{\sin u}{b}\right)^p}}\cos u \\ y(u,v) &= \frac{v}{\sqrt[p]{\left(\frac{\cos u}{a}\right)^p + \left(\frac{\sin u}{b}\right)^p}}\sin u \end{aligned}\right\} \begin{matrix} \pi/2 \le u \le \pi \\ 1-d/a \le v \le 1 \end{matrix} \quad (4)$$

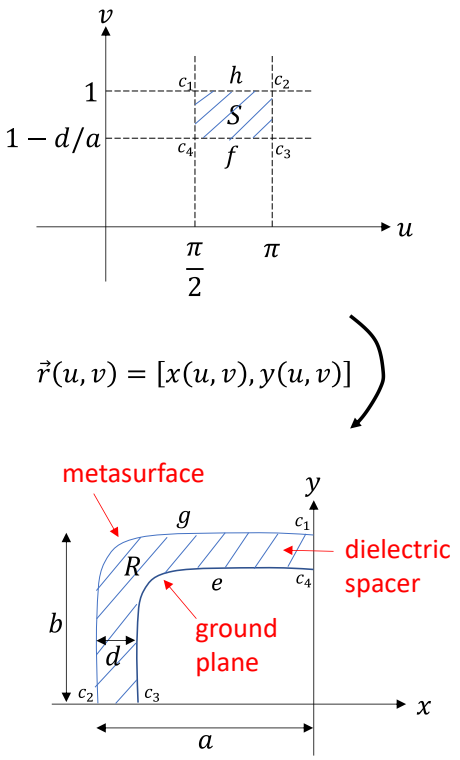

Fig. 11. Parameterization of conformal metasurface.

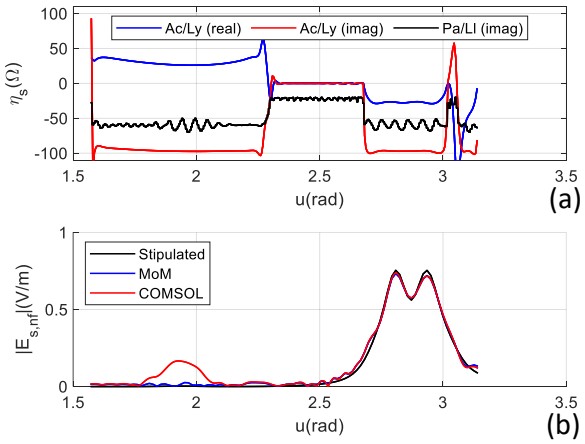

Fig. 12. (a) Metasurface sheet impedances of initial local active/lossy (Ac/Ly) metasurface design, and subsequent non-local passive and lossless (Pa/Ll) design vs. parameter u. (b) Line cut of near electric scattered field amplitude at a height of one wavelength above the metasurface.

The parameterization is also shown graphically in Fig. 11. The parameters a and b control the aperture length along the x-axis and y-axis, respectively, and the parameter d controls the substrate thickness. The parameter p controls the metasurface shape and radius of curvature at the bend. For $p = 2$, for example, (4) defines a quadrant of a circular annulus in the xy-plane. As $p \to \infty$, the parameterization approaches a quadrant of a square ring with thickness d. When $v = 1$, the superquadric has the largest radius (the curve g in Fig. 11). The impedance

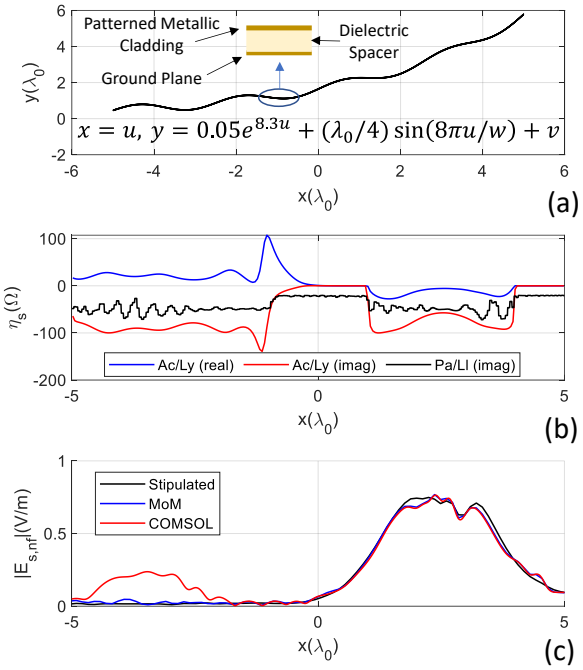

Fig. 13. (a) Conformal metasurface geometry. (b) Metasurface sheet impedances of initial local active/lossy (Ac/Ly) metasurface design, and subsequent non-local passive and lossless (Pa/Ll). (c) Line cut of near electric scattered field amplitude at a height of one wavelength above the metasurface.

sheet will be placed along this arc. When $v = 1 - d/a$, the superquadric has the smallest radius (the curve e in Fig. 11). This is where the perfectly conducting ground plane will be placed. $\forall v$ between these two values, the space between is filled (the dielectric material of the substrate will fill this area). For the parameters in (4), the greatest radius of curvature calculated using (11) at the 90° bend point is $R = 0.587\lambda_0$. The metasurface has length $a = 8\lambda_0$ along the x-axis, $b = 8\lambda_0$ along the y-axis, and thickness $d = 1.27$mm (50mil). It is constructed from the same three layer stack: a patterned metallic cladding represented as a spatially variant homogenized impedance sheet, a dielectric spacer, and a ground plane. The incident field is a Gaussian beam again with a waist radius of $w_0 = \lambda_0$. For this case, the center of the waist is located at $x = -3.5\lambda_0$ and $y = b$. The Gaussian beam will be absorbed at this space wave port and converted into a surface wave. The surface wave will travel around the bend delivering the power to port 2 defined along $\lambda_0 \le y \le 4\lambda_0$, where it will be reformed into a collimated beam corresponding to an aperture field with uniform amplitude and phase. Both the MATLAB design codes and the COMSOL Multiphysics verification models for this design are available through the IEEE DataPort at [19].

Figure 12a shows the metasurface sheet impedances for both the local active/lossy metasurface design and the non-local passive/lossless metasurface design. Figure 12b shows the near field amplitude taken along a contour following the metasurface and one wavelength above the metasurface. As can be seen, the non-local passive/lossless metasurface performs identically to the local active/lossy design. Finally, the real part of the total near electric field is shown in Fig. 10b. As in the planar case,

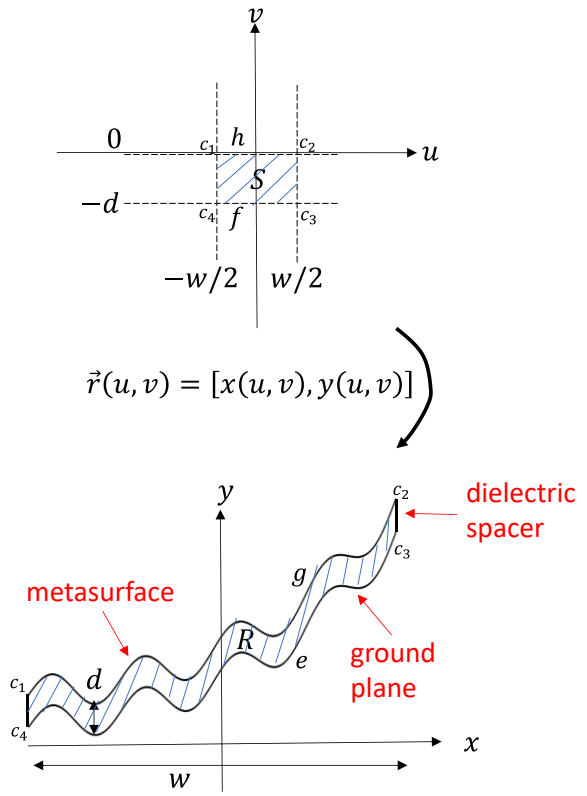

Fig. 14. Parameterization of conformal metasurface.

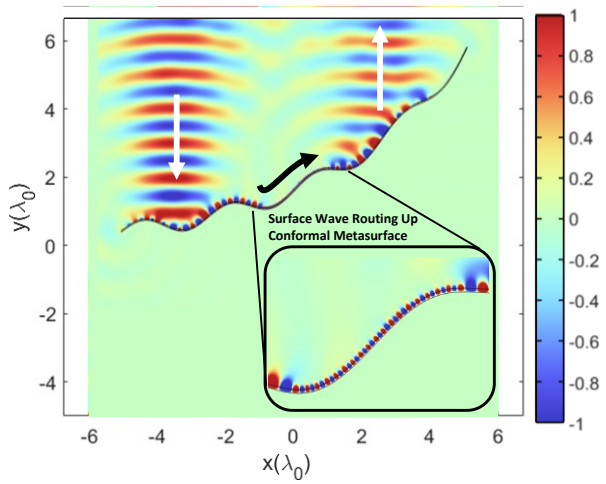

Fig. 15. COMSOL Multiphysics simulation results of a conformal transporting metasurface shaped using a sinusoid added to an exponential function.

the metasurface is performing the function of near perfect space wave transportation, only in this case, the space wave beam is seen to transport around the corner of a building.

B. Sinusoidally Modulated Exponential Metasurface Coupler

The final example is a near perfect conformal wave transporting metasurface where the coupling regions are not planar. The geometry and its parameterization are shown in Fig. 13a and in Fig. 14, respectively. The parameterization can be described as a sinusoidally modulated exponential

$$\left.\begin{aligned} x(u,v) &= u \\ y(u,v) &= ce^{au} + p\sin bu + v \end{aligned}\right\} \begin{aligned} -w/2 \le u \le w/2 \\ -d \le v \le 0 \end{aligned} \quad (5)$$

The parameter w controls the aperture length along the x-axis, and the parameter d controls the substrate thickness. The parameters c and a controls the amplitude and the growth rate of the exponential function, which acts as a fundamental term of which the sinusoid is added to. The parameters p and b control the amplitude and period of the sinusoidal term. The impedance sheet will be placed along the curve resulting from $v = 0$, The perfectly conducting ground plane will be placed along the curve at $v = -d$. $\forall v$ between these two values, the space between is filled (the dielectric material of the substrate will fill this area). The metasurface width, as projected onto the x-axis, is $w = 10\lambda_0$. The incident field is again a Gaussian beam with a waist radius of $w_0 = \lambda_0$. For this case, the center of the waist is located at $x = -3.5\lambda_0$ and $y = \lambda_0$. Defining the scattered field as $E_z^{sca} = e^{-jky}$, for $\lambda_0 \le x \le 4\lambda_0$, and solving the governing integral equation, results in the active/lossy design impedances shown in Fig. 13b. The corresponding passive/lossless design's reactances after optimization are also shown in Fig. 13b. Finally, the COMSOL Multiphysics simulation results of the real part of the total near electric field for the Gaussian beam excited passive/lossless design is shown in Fig. 15. Wave transportation is again observed, as well as near perfect coupling of a normally incident plane wave to a surface wave over a conformal surface. In Fig. 13c, the magnitude of the electric near field is plotted along a contour the same shape as the metasurface displaced one wavelength above it. The figure shows some imperfect coupling in the COMSOL Multiphysics result and/or impedance matching between the port region and the tunnel region as some scattered electric field is present over the input port region. This may be due to the paraxial approximation for the Gaussian beam used in the MoM whereas in COMSOL Multiphysics, a more accurate representation based on a plane wave decomposition is used. Nonetheless, the full-wave results again corroborate our results.

Note, both the MATLAB design codes and the COMSOL Multiphysics verification models for this design are also available through the IEEE DataPort at [19].

V. Conclusion

Conformal, metasurface-based, space-wave to surface-wave couplers were designed to transport a space wave from one location in space to another via surface wave and reradiate it as a newly formed beam. The reradiated space wave can be formed into an arbitrary beam with control over its amplitude and phase. The metasurfaces can conform to any shape, are fully passive and lossless, and hence require no powered connections. The metasurfaces are deemed near-perfect, as over 97.5% of the available power in the incident space wave is transported to the output wave in all cases. These types of metasurfaces can be useful to fill in hard to reach shadow zones in new high-frequency communications systems in an efficient, power-free manner. The conformal metasurfaces are designed using a coupled system of integral equations formulated for arbitrarily shaped geometries defined parametrically. The integral equations are solved via the method of moments. All

design codes and full-wave simulation files used for validation are available as supplementary materials.

Finally, note the primary purpose of this paper is to show that near perfect transportation is possible and what the sheet impedances look like. Support for dielectric materials is currently being added to the unit cell design process required to realize these metasurfaces outlined in [20]. Once this is complete, follow-on work involves translating the optimized impedance sheets for all designs in this paper to patterned metallic claddings.

APPENDIX A: METHOD OF MOMENTS FOR PARAMETERIZED GEOMETRIES

A. Integral Equations for Conformal Geometry

The conformal upgrade of the integral equation in [9]–[11] involves both line and area integrations over the boundary and domain of the region R in Fig. 11 and Fig. 14, respectively. Single integrals over curves bounding the region R (curve g or e in Fig. 11 for example) can be evaluated by integrating over curves bounding the parameter space region S (curve h or f in Fig. 11 for example) from

$$\int_{g,e} f(x,y)ds = \int_{h,f} f(x(u,v_0),y(u,v_0))\sqrt{\left(\left.\frac{\partial x}{\partial u}\right|_{v=v_0}\right)^2+\left(\left.\frac{\partial y}{\partial u}\right|_{v=v_0}\right)^2}\,du \tag{6}$$

where $v_0 = 1$ or $1-d/a$ for integration over the metasurface layer (curves g or h) or ground plane layer (curves e or f), respectively. To evaluate the double integrals over the region R, the integrations can be done over the region S in the parameter space using

$$\iint_R f(x,y)dA = \iint_S f(x(u,v),y(u,v))\left|\begin{matrix}\partial x/\partial u & \partial y/\partial u\\ \partial x/\partial v & \partial y/\partial v\end{matrix}\right|dudv \tag{7}$$

Care must be taken to ensure the absolute value of the Jacobian determinant appearing in (7) is always taken (note, the Jacobian determinant associated with the mapping in Fig. 11 turns out to be negative so the absolute value must be taken).

The integral equations will be derived for the parametric geometry in Fig. 11. Those for any other geometry can be found analogously. The metasurface can be modeled as consisting of three layers, denoted by different values of v_0. Layer 1, at $v_0 = 1$ denotes the impedance sheet. Layer 2, at $v_0 = v$, denotes the dielectric spacer. Layer 3, at $v_0 = 1-d/a$, denotes the perfectly conducting ground plane. An integral equation can be constructed for each layer, and hence there are three total integral equations, one for each choice of v_0 in the following

$$\begin{aligned}
&E^i\left(x(u,v_0),y(u,v_0)\right) = \eta_s\left(x(u,v_0),y(u,v_0)\right)J\left(x(u,v_0),y(u,v_0)\right)\\
&+\frac{\eta_0 k_0}{4}\int_{u'=\pi/2}^{u'=\pi} H_0^{(2)}\left(k_0\sqrt{\left[x(u,v_0)-x(u',1)\right]^2+\left[y(u,v_0)-y(u',1)\right]^2}\right)\\
&\qquad J\left(x(u',1),y(u',1)\right)\sqrt{\left(\left.\frac{\partial x}{\partial u'}\right|_{v'=1}\right)^2+\left(\left.\frac{\partial y}{\partial u'}\right|_{v'=1}\right)^2}\,du'\\
&+\frac{\eta_0 k_0}{4}\int_{v'=1-d/a}^{v'=1}\int_{u'=\pi/2}^{u'=\pi} H_0^{(2)}\left(k_0\sqrt{\left[x(u,v_0)-x(u',v')\right]^2+\left[y(u,v_0)-y(u',v')\right]^2}\right)\\
&\qquad J\left(x(u',v'),y(u',v')\right)\left|\begin{matrix}\partial x/\partial u' & \partial y/\partial u'\\ \partial x/\partial v' & \partial y/\partial v'\end{matrix}\right|du'dv'\\
&+\frac{\eta_0 k_0}{4}\int_{u'=\pi/2}^{u'=\pi} H_0^{(2)}\left(k_0\sqrt{\left[x(u,v_0)-x(u',1-d/a)\right]^2+\left[y(u,v_0)-y(u',1-d/a)\right]^2}\right)\\
&\qquad J\left(x(u',1-d/a),y(u',1-d/a)\right)\sqrt{\left(\left.\frac{\partial x}{\partial u'}\right|_{v'=1-d/a}\right)^2+\left(\left.\frac{\partial y}{\partial u'}\right|_{v'=1-d/a}\right)^2}\,du'
\end{aligned} \tag{8}$$

The three integral equations in (8) (one for each choice of v_0) can be simultaneously solved by the method of moments as presented in the next section.

The derivatives of (4) and (5) are also useful. For (4), they are

$$\begin{aligned}
\frac{\partial x}{\partial u} &= \frac{-v}{\sqrt[p]{\left(\frac{\cos u}{a}\right)^p+\left(\frac{\sin u}{b}\right)^p}}\sin u - \frac{v}{\left[\left(\frac{\cos u}{a}\right)^p+\left(\frac{\sin u}{b}\right)^p\right]^{\frac{1}{p}+1}}\\
&\times\left(\left(\frac{\cos u}{a}\right)^{p-1}\left(\frac{-\sin u}{a}\right)+\left(\frac{\sin u}{b}\right)^{p-1}\left(\frac{\cos u}{b}\right)\right)\cos u\\
\frac{\partial y}{\partial u} &= \frac{v}{\sqrt[p]{\left(\frac{\cos u}{a}\right)^p+\left(\frac{\sin u}{b}\right)^p}}\cos u - \frac{v}{\left[\left(\frac{\cos u}{a}\right)^p+\left(\frac{\sin u}{b}\right)^p\right]^{\frac{1}{p}+1}}\\
&\times\left(\left(\frac{\cos u}{a}\right)^{p-1}\left(\frac{-\sin u}{a}\right)+\left(\frac{\sin u}{b}\right)^{p-1}\left(\frac{\cos u}{b}\right)\right)\sin u\\
\frac{\partial x}{\partial v} &= \frac{1}{\sqrt[p]{\left(\frac{\cos u}{a}\right)^p+\left(\frac{\sin u}{b}\right)^p}}\cos u\\
\frac{\partial y}{\partial v} &= \frac{1}{\sqrt[p]{\left(\frac{\cos u}{a}\right)^p+\left(\frac{\sin u}{b}\right)^p}}\sin u
\end{aligned} \tag{9}$$

The derivatives of (5) are are

$$\frac{\partial x}{\partial u} = 1, \quad \frac{\partial y}{\partial u} = cae^{au} + pb\cos bu, \quad \frac{\partial x}{\partial v} = 0, \quad \frac{\partial y}{\partial v} = 1 \tag{10}$$

Also the curvature, κ, of the impedance sheet layer can be computed from

$$\kappa(u)=\frac{\left|\vec{r}'(u,1)\times\vec{r}''(u,1)\right|}{\left|\vec{r}'(u,1)\right|^3}$$
$$\vec{r}'=\left[\frac{\partial}{\partial u}x(u,1),\frac{\partial}{\partial u}y(u,1)\right] \quad (11)$$
$$\vec{r}''=\left[\frac{\partial^2}{\partial u^2}x(u,1),\frac{\partial^2}{\partial u^2}y(u,1)\right]$$

B. Method of Moment Solution of Integral Equations

The current densities in (8) are expanded into pulse basis functions placed in the parametric space tessellating the domain and boundary of S (1D pulses for the boundary of S mapping electric surface current densities on the metasurface and ground plane, and 2D pulses for the area within S mapping polarization current densities in the dielectric substrate)

$$\begin{aligned}
J_1(u)&=J_1\left(x(u,1),y(u,1)\right)\\
&=\sum_{n=1}^{N_1}\alpha_n P_n\left(x(u,1),y(u,1)\right),\ |u-u_n|\le\frac{\Delta u_n}{2}\\
J_2(u,v)&=J_2\left(x(u,v),y(u,v)\right)\\
&=\sum_{n=1}^{N_2}\alpha_n P_n\left(x(u,v),y(u,v)\right),\ |u-u_n|\le\frac{\Delta u_n}{2},\ |v-v_n|\le\frac{\Delta v_n}{2}\\
J_3(u)&=J_3\left(x(u,1-d/a),y(u,1-d/a)\right)\\
&=\sum_{n=1}^{N_3}\alpha_n P_n\left(x(u,1-d/a),y(u,1-d/a)\right),\ |u-u_n|\le\frac{\Delta u_n}{2}
\end{aligned} \quad (12)$$

Δu_n denotes the width of the nth basis function and Δv_n denotes its height in the 2D case. Note, the Δu_n are chosen such that the arc length of the unit cells in the parameterized curve are of equal arc length. Substitution of (12) into (8) and testing the integral equation using the same expansion functions (Galerkin method) results in (for $v_0=1$ for example)

$$\begin{aligned}
&\int_{u=u_m-\Delta u/2}^{u=u_m+\Delta u/2}E^i\left(x(u,1),y(u,1)\right)\sqrt{\left(\frac{\partial x}{\partial u}\Big|_{v=1}\right)^2+\left(\frac{\partial y}{\partial u}\Big|_{v=1}\right)^2}\,du\\
&=\eta_s\left(x(u,1),y(u,1)\right)\sum_{n=1}^{N_1}\alpha_n\int_{u=u_m-\Delta u/2}^{u=u_m+\Delta u/2}\delta_{mn}\sqrt{\left(\frac{\partial x}{\partial u}\Big|_{v=1}\right)^2+\left(\frac{\partial y}{\partial u}\Big|_{v=1}\right)^2}\,du\\
&+\frac{\eta_0k_0}{4}\sum_{n=1}^{N_1}\alpha_n\int_{u=u_m-\Delta u/2}^{u=u_m+\Delta u/2}\int_{u'=u_n-\Delta u/2}^{u'=u_n+\Delta u/2}H_0^{(2)}\left(k_0\sqrt{\left[x(u,1)-x(u',1)\right]^2+\left[y(u,1)-y(u',1)\right]^2}\right)\\
&\qquad\sqrt{\left(\frac{\partial x}{\partial u'}\Big|_{v=1}\right)^2+\left(\frac{\partial y}{\partial u'}\Big|_{v=1}\right)^2}\sqrt{\left(\frac{\partial x}{\partial u}\Big|_{v=1}\right)^2+\left(\frac{\partial y}{\partial u}\Big|_{v=1}\right)^2}\,du'\,du\\
&+\frac{\eta_0k_0}{4}\sum_{n=1}^{N_2}\alpha_n\int_{u=u_m-\Delta u/2}^{u=u_m+\Delta u/2}\int_{v'=v_n-\Delta v/2}^{v'=v_n+\Delta v/2}\int_{u'=u_n-\Delta u/2}^{u'=u_n+\Delta u/2}H_0^{(2)}\left(k_0\sqrt{\left[x(u,1)-x(u',v')\right]^2+\left[y(u,1)-y(u',v')\right]^2}\right)\\
&\qquad\left|\begin{matrix}\partial x/\partial u' & \partial y/\partial u'\\ \partial x/\partial v' & \partial y/\partial v'\end{matrix}\right|\sqrt{\left(\frac{\partial x}{\partial u}\Big|_{v=1}\right)^2+\left(\frac{\partial y}{\partial u}\Big|_{v=1}\right)^2}\,du'\,dv'\,du\\
&+\frac{\eta_0k_0}{4}\sum_{n=1}^{N_3}\alpha_n\int_{u=u_m-\Delta u/2}^{u=u_m+\Delta u/2}\int_{u'=u_n-\Delta u/2}^{u'=u_n+\Delta u/2}H_0^{(2)}\left(k_0\sqrt{\left[x(u,1)-x(u',1-d/a)\right]^2+\left[y(u,1)-y(u',1-d/a)\right]^2}\right)\\
&\qquad\sqrt{\left(\frac{\partial x}{\partial u'}\Big|_{v=1-d/a}\right)^2+\left(\frac{\partial y}{\partial u'}\Big|_{v=1-d/a}\right)^2}\sqrt{\left(\frac{\partial x}{\partial u}\Big|_{v=1}\right)^2+\left(\frac{\partial y}{\partial u}\Big|_{v=1}\right)^2}\,du'\,du
\end{aligned} \quad (13)$$

The integral equation in (13) can be written in the following form $V_1=Z_{s1}I_1+Z_{11}I_1+Z_{12}I_2+Z_{13}I_3=(Z_{11}+Z_{s1})I_1+Z_{12}I_2+Z_{13}I_3$, where

$$\begin{aligned}
[V_1]_{N_1\times1}&=\int_{u=u_m-\Delta u/2}^{u=u_m+\Delta u/2}E^i\left(x(u,1),y(u,1)\right)\sqrt{\left(\frac{\partial x}{\partial u}\Big|_{v=1}\right)^2+\left(\frac{\partial y}{\partial u}\Big|_{v=1}\right)^2}\,du\\
[Z_{s1}]_{N_1\times N_1}&=\eta_s\left(x(u,1),y(u,1)\right)\int_{u=u_m-\Delta u/2}^{u=u_m+\Delta u/2}\delta_{mn}\sqrt{\left(\frac{\partial x}{\partial u}\Big|_{v=1}\right)^2+\left(\frac{\partial y}{\partial u}\Big|_{v=1}\right)^2}\,du\\
[Z_{11}]_{N_1\times N_1}&=\frac{\eta_0k_0}{4}\int_{u=u_m-\Delta u/2}^{u=u_m+\Delta u/2}\int_{u'=u_n-\Delta u/2}^{u'=u_n+\Delta u/2}H_0^{(2)}\left(k_0\sqrt{\left[x(u,1)-x(u',1)\right]^2+\left[y(u,1)-y(u',1)\right]^2}\right)\\
&\qquad\sqrt{\left(\frac{\partial x}{\partial u'}\Big|_{v=1}\right)^2+\left(\frac{\partial y}{\partial u'}\Big|_{v=1}\right)^2}\sqrt{\left(\frac{\partial x}{\partial u}\Big|_{v=1}\right)^2+\left(\frac{\partial y}{\partial u}\Big|_{v=1}\right)^2}\,du'\,du\\
[Z_{12}]_{N_1\times N_2}&=\frac{\eta_0k_0}{4}\int_{u=u_m-\Delta u/2}^{u=u_m+\Delta u/2}\int_{v'=v_n-\Delta v/2}^{v'=v_n+\Delta v/2}\int_{u'=u_n-\Delta u/2}^{u'=u_n+\Delta u/2}H_0^{(2)}\left(k_0\sqrt{\left[x(u,1)-x(u',v')\right]^2+\left[y(u,1)-y(u',v')\right]^2}\right)\\
&\qquad\left|\begin{matrix}\partial x/\partial u' & \partial y/\partial u'\\ \partial x/\partial v' & \partial y/\partial v'\end{matrix}\right|\sqrt{\left(\frac{\partial x}{\partial u}\Big|_{v=1}\right)^2+\left(\frac{\partial y}{\partial u}\Big|_{v=1}\right)^2}\,du'\,dv'\,du\\
[Z_{13}]_{N_1\times N_3}&=\frac{\eta_0k_0}{4}\int_{u=u_m-\Delta u/2}^{u=u_m+\Delta u/2}\int_{u'=u_n-\Delta u/2}^{u'=u_n+\Delta u/2}H_0^{(2)}\left(k_0\sqrt{\left[x(u,1)-x(u',1-d/a)\right]^2+\left[y(u,1)-y(u',1-d/a)\right]^2}\right)\\
&\qquad\sqrt{\left(\frac{\partial x}{\partial u'}\Big|_{v=1-d/a}\right)^2+\left(\frac{\partial y}{\partial u'}\Big|_{v=1-d/a}\right)^2}\sqrt{\left(\frac{\partial x}{\partial u}\Big|_{v=1}\right)^2+\left(\frac{\partial y}{\partial u}\Big|_{v=1}\right)^2}\,du'\,du\\
[I_1]_{N_1\times1}&=\alpha_{n1}\\
[I_2]_{N_2\times1}&=\alpha_{n2}\\
[I_3]_{N_3\times1}&=\alpha_{n3}
\end{aligned} \quad (14)$$

The self terms ($m=n$) in (14) are calculated using the procedure outlined in [21]. For completeness and since those formulas are adapted to the conformal parametric geometry case, the formulas for calculating the self-terms are provided in the next section. Following the same procedure for the remaining layers ($v_0=v$ for layer 2 and $v_0=1-d/a$ for layer 3) leads to the block matrix equation

$$\begin{bmatrix}V_1\\V_2\\V_3\end{bmatrix}=\begin{bmatrix}Z_{11}+Z_{s1} & Z_{12} & Z_{13}\\ Z_{21} & Z_{22}+Z_v & Z_{23}\\ Z_{31} & Z_{32} & Z_{33}\end{bmatrix}\begin{bmatrix}I_1\\I_2\\I_3\end{bmatrix} \quad (15)$$

Note, for the dielectric layer, $Z_v=eye([j\omega\epsilon_0(\epsilon_r-1)]^{-1})$, where eye( ) indicates an identity matrix with the argument appearing along the diagonal. Also note, $\eta_s=0$ for layer 3 and hence Z_{s3} does not appear in (15). Finally, note in our implementation, each of the voltage vector and impedance matrix elements in (14) are normalized to their own arc length (for 1D) or area (for 2D).

The matrix equation (15) can be solved by either knowing the sheet impedances Z_{s1} (as in each iteration of the optimization phase leading to the passive/lossless design) or by knowing the desired total field and making the substitution $W_1=Z_{s1}I_1$ following from the boundary condition $E^{tot}=\eta_sJ_1$ (as in the initial solve phase leading to the active/lossy design)

$$\begin{bmatrix}V-W_1\\V_2\\V_3\end{bmatrix}=\begin{bmatrix}Z_{11} & Z_{12} & Z_{13}\\ Z_{21} & Z_{22}+Z_v & Z_{23}\\ Z_{31} & Z_{32} & Z_{33}\end{bmatrix}\begin{bmatrix}I_1\\I_2\\I_3\end{bmatrix} \quad (16)$$

Since, in our case, the desired total field, E^t, is known, the W_1 vector can be found from

$$W_1=\int_{u=u_m-\Delta u/2}^{u=u_m+\Delta u/2}E^t\left(x(u,1),y(u,1)\right)\sqrt{\left(\frac{\partial x}{\partial u}\Big|_{v=1}\right)^2+\left(\frac{\partial y}{\partial u}\Big|_{v=1}\right)^2}\,du \quad (17)$$

In this case, after solving equation (16) for the current I_1, the complex-valued sheet impedances can be found by returning back to the boundary condition from $\eta_s = W_1/I_1$.

C. Calculation of Singular Matrix Element Terms

The self terms ($m = n$) in (14) are calculated using the procedure outlined in [21]. We summarize their results here adapted to our case of conformal method of moments. For more details, refer to the original paper [21]. There are two types of singular integrals, the surface integrals (associated with $[Z_{11}]$ and $[Z_{33}]$) and the volume integrals (associated with $[Z_{22}]$). We treat the surface integrals first.

Singular Surface Integrals

The integral in question (for $[Z_{11}]$ for example) is

$$I_s = \frac{\eta_0 k_0}{4}\int_{u=u_m-\Delta u/2}^{u=u_m+\Delta u/2}\int_{u'=u_n-\Delta u/2}^{u'=u_n+\Delta u/2} H_0^{(2)}\left(k_0\sqrt{\left[x(u,1)-x(u',1)\right]^2+\left[y(u,1)-y(u',1)\right]^2}\right) \sqrt{\left(\left.\frac{\partial x}{\partial u'}\right|_{v=1}\right)^2+\left(\left.\frac{\partial y}{\partial u'}\right|_{v=1}\right)^2}\sqrt{\left(\left.\frac{\partial x}{\partial u}\right|_{v=1}\right)^2+\left(\left.\frac{\partial y}{\partial u}\right|_{v=1}\right)^2}\,du'\,du \tag{18}$$

By singularity subtraction, the Hankel function can be written as

$$H_0^{(2)}(k_0P) = \left[H_0^{(2)}(k_0P) + j\frac{2}{\pi}\ln P\right] - j\frac{2}{\pi}\ln P \tag{19}$$

where $P = \sqrt{\left(x(u,1)-x(u',1)\right)^2+\left(y(u,1)-y(u',1)\right)^2}$.

The first term in the brackets is well-behaved and can be integrated numerically. The strategy for the remaining term is to perform the inner integration analytically assuming a variable observation point u passed in from the outer integral, then integrate the outer integral numerically using the analytic result from the inner integral as the integrand.

$$\begin{aligned} I_s &= \frac{\eta_0 k_0}{4}\int_{u=u_m-\Delta u/2}^{u=u_m+\Delta u/2}\int_{u'=u_n-\Delta u/2}^{u'=u_n+\Delta u/2}\left[H_0^{(2)}(k_0P)+j\frac{2}{\pi}\ln P\right] \\ &\times\sqrt{\left(\left.\frac{\partial x}{\partial u'}\right|_{v=1}\right)^2+\left(\left.\frac{\partial y}{\partial u'}\right|_{v=1}\right)^2}\sqrt{\left(\left.\frac{\partial x}{\partial u}\right|_{v=1}\right)^2+\left(\left.\frac{\partial y}{\partial u}\right|_{v=1}\right)^2}\,du'\,du \\ &-j\frac{\eta_0 k_0}{2\pi}\int_{u=u_m-\Delta u/2}^{u=u_m+\Delta u/2}\left[\int_{u'=u_n-\Delta u/2}^{u'=u_n+\Delta u/2}\ln P\sqrt{\left(\left.\frac{\partial x}{\partial u'}\right|_{v=1}\right)^2+\left(\left.\frac{\partial y}{\partial u'}\right|_{v=1}\right)^2}\,du'\right] \\ &\times\sqrt{\left(\left.\frac{\partial x}{\partial u}\right|_{v=1}\right)^2+\left(\left.\frac{\partial y}{\partial u}\right|_{v=1}\right)^2}\,du \\ &= I_{s1}+I_{s2} \end{aligned} \tag{20}$$

The inner integral of I_{s2} (in brackets) to integrate analytically becomes

$$I_{s2,in}(u) = \int_{u'=u_n-\Delta u/2}^{u'=u_n+\Delta u/2}\ln P\sqrt{\left(\left.\frac{\partial x}{\partial u'}\right|_{v=1}\right)^2+\left(\left.\frac{\partial y}{\partial u'}\right|_{v=1}\right)^2}\,du' \tag{21}$$

With reference to Fig. 16, the coordinate origin is denoted by O. The observation point position vector is denoted by $\vec{\rho} = [x(u,1), y(u,1)]$. The source point position vector is denoted by $\vec{\rho}' = [x(u',1), y(u',1)]$. The source line segment, C, is colored red in Fig. 16 and is parameterized by the arc length variable l' measured from the line perpendicular to the extension of C and which passes through the point located by $\vec{\rho}$. The endpoints of the source segment are pointed to by the vectors $\vec{\rho}'^{-}$ and $\vec{\rho}'^{+}$. The coordinates P^0 and l' can be considered a pair of rectangular coordinates with origin at $\vec{\rho}$, locating points on the line segment C. Thus, the endpoints of the source segment are located at a distance of

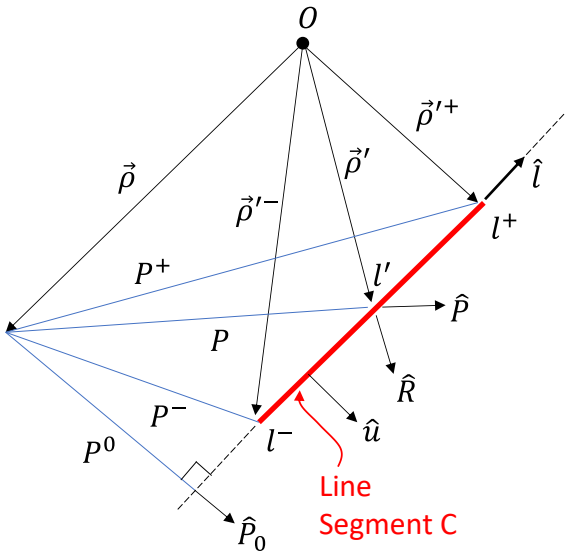

Fig. 16. Geometrical definitions for analytic line integration.

$$P^{\pm} = \left|\vec{\rho}^{\pm} - \vec{\rho}\right| = \sqrt{\left(P^0\right)^2+\left(l^{\pm}\right)^2} \tag{22}$$

Other quantities in Fig. 16 are given by

$$\begin{aligned} \hat{l} &= \frac{\vec{\rho}^{+}-\vec{\rho}^{-}}{\left|\vec{\rho}^{+}-\vec{\rho}^{-}\right|} \\ u &= \hat{l}\times n = \hat{l}\times\hat{z} \\ l^{\pm} &= \left(\vec{\rho}^{\pm}-\vec{\rho}\right)\bullet\hat{l} \\ P^0 &= \left|\left(\vec{\rho}^{\pm}-\vec{\rho}\right)\bullet u\right| \\ P^0 &= \frac{\left(\vec{\rho}^{\pm}-\vec{\rho}\right)-l^{\pm}\hat{l}}{P^0} \end{aligned} \tag{23}$$

All quantities in (22) and (23) can be solved for once $\vec{\rho}$ (the observation point) and $\vec{\rho}^{\pm}$ (the source segment endpoints) are defined. By defining

$$\begin{aligned} \vec{\rho} &= [x(u,1), y(u,1)] \\ \vec{\rho}^{-} &= [x(u_n-\Delta u/2,1), y(u_n-\Delta u/2,1)] \\ \vec{\rho}^{+} &= [x(u_n+\Delta u/2,1), y(u_n+\Delta u/2,1)] \end{aligned} \tag{24}$$

the integration is done in the xy-space using the above paradigm rather than over the parametric uv-space since the vectors in (24) are constant (see Fig. 11). Thus, (21) becomes

$$I_{s2,in}(u)=\int_C \ln P\,dl'=\int_{l^-}^{l^+}\ln\sqrt{\left(P^0\right)^2+\left(l'\right)^2}\,dl'$$
$$=l^+\ln P^+-l^-\ln P^- \quad (25)$$
$$+P^0\left(\tan^{-1}\left(\frac{l^+}{P^0}\right)-\tan^{-1}\left(\frac{l^-}{P^0}\right)\right)-\left(l^+-l^-\right)$$

The result in (25) can be singular if $P^{\pm}=0$, which happens when the observation point $\vec{\rho}$ lies on either of the endpoints of the line segment C. In this case, the observation point can be set to $\vec{\rho}=\vec{\rho}+\epsilon\hat{u}$, where ϵ is a small constant. The complete integral (20) can now be evaluated numerically as

$$I_s=\frac{\eta_0 k_0}{4}\int_{u=u_m-\Delta u/2}^{u=u_m+\Delta u/2}\int_{u'=u_n-\Delta u/2}^{u'=u_n+\Delta u/2}\left[1-j\frac{2}{\pi}\ln\left(\frac{\gamma}{2}k_0\right)\right]$$
$$\times\sqrt{\left(\left.\frac{\partial x}{\partial u'}\right|_{v=1}\right)^2+\left(\left.\frac{\partial y}{\partial u'}\right|_{v=1}\right)^2}\sqrt{\left(\left.\frac{\partial x}{\partial u}\right|_{v=1}\right)^2+\left(\left.\frac{\partial y}{\partial u}\right|_{v=1}\right)^2}\,du'du$$
$$-j\frac{\eta_0 k_0}{2\pi}\int_{u=u_m-\Delta u/2}^{u=u_m+\Delta u/2} I_{s2,in}(u)\sqrt{\left(\left.\frac{\partial x}{\partial u}\right|_{v=1}\right)^2+\left(\left.\frac{\partial y}{\partial u}\right|_{v=1}\right)^2}\,du \quad (26)$$

where $\gamma=1.781$ and since $\left[H_0^{(2)}(k_0P)+j\frac{2}{\pi}\ln P\right]=1-j\frac{2}{\pi}\ln\left(\frac{\gamma}{2}k_0\right)$ by the small argument expansion for the Hankel function. A similar approach is used for the singular terms of $[Z_{33}]$. This completes the singular surface integral calculation. The singular volume integrals are handled next.

Singular Volume Integrals

The integral in question is

$$I_v=\frac{\eta_0 k_0}{4}\int_{v=v_m-\Delta v/2}^{v=v_m+\Delta v/2}\int_{u=u_m-\Delta u/2}^{u=u_m+\Delta u/2}\int_{v'=v_n-\Delta v/2}^{v'=v_n+\Delta v/2}\int_{u'=u_n-\Delta u/2}^{u'=u_n+\Delta u/2} H_0^{(2)}\left(k_0\sqrt{\left[x(u,v)-x(u',v')\right]^2+\left[y(u,v)-y(u',v')\right]^2}\right)$$
$$\left|\begin{matrix}\partial x/\partial u' & \partial y/\partial u'\\ \partial x/\partial v' & \partial y/\partial v'\end{matrix}\right|\left|\begin{matrix}\partial x/\partial u & \partial y/\partial u\\ \partial x/\partial v & \partial y/\partial v\end{matrix}\right|du'dv'dudv \quad (27)$$

Using the singularity subtraction technique, (27) becomes

$$I_v=\frac{\eta_0 k_0}{4}\int_{v=v_m-\Delta v/2}^{v=v_m+\Delta v/2}\int_{u=u_m-\Delta u/2}^{u=u_m+\Delta u/2}\int_{v'=v_n-\Delta v/2}^{v'=v_n+\Delta v/2}\int_{u'=u_n-\Delta u/2}^{u'=u_n+\Delta u/2}\left[1-j\frac{2}{\pi}\ln\left(\frac{\gamma}{2}k_0\right)\right]$$
$$\times\left|\begin{matrix}\partial x/\partial u' & \partial y/\partial u'\\ \partial x/\partial v' & \partial y/\partial v'\end{matrix}\right|\left|\begin{matrix}\partial x/\partial u & \partial y/\partial u\\ \partial x/\partial v & \partial y/\partial v\end{matrix}\right|du'dv'dudv$$
$$-j\frac{\eta_0 k_0}{2\pi}\int_{v=v_m-\Delta v/2}^{v=v_m+\Delta v/2}\int_{u=u_m-\Delta u/2}^{u=u_m+\Delta u/2}\int_{v'=v_n-\Delta v/2}^{v'=v_n+\Delta v/2}\int_{u'=u_n-\Delta u/2}^{u'=u_n+\Delta u/2}\ln P\left|\begin{matrix}\partial x/\partial u' & \partial y/\partial u'\\ \partial x/\partial v' & \partial y/\partial v'\end{matrix}\right|$$
$$\times\left|\begin{matrix}\partial x/\partial u & \partial y/\partial u\\ \partial x/\partial v & \partial y/\partial v\end{matrix}\right|du'dv'dudv$$
$$=I_{v1}+I_{v2} \quad (28)$$

where $P=\sqrt{\left(x(u,v)-x(u',v')\right)^2+\left(y(u,v)-y(u',v')\right)^2}$.

Integral I_{v1} can be integrated numerically. Integral I_{v2} will be integrated analytically for the inner integral and numerically for the outer integral.

$$I_{v2}=-j\frac{\eta_0 k_0}{2\pi}\int_{v=v_m-\Delta v/2}^{v=v_m+\Delta v/2}\int_{u=u_m-\Delta u/2}^{u=u_m+\Delta u/2}\left[\int_{v'=v_n-\Delta v/2}^{v'=v_n+\Delta v/2}\int_{u'=u_n-\Delta u/2}^{u'=u_n+\Delta u/2}\ln P\right.$$
$$\left.\times\left|\begin{matrix}\partial x/\partial u' & \partial y/\partial u'\\ \partial x/\partial v' & \partial y/\partial v'\end{matrix}\right|du'dv'\right]\left|\begin{matrix}\partial x/\partial u & \partial y/\partial u\\ \partial x/\partial v & \partial y/\partial v\end{matrix}\right|dudv \quad (29)$$

Again, the term in brackets will be labeled the inner integral, $I_{v2,in}$. To integrate $I_{v2,in}$ analytically, we employ a Gauss integral theorem. Thus, in the xy-space, we express the integrand as

$$I_{2v,in}=\int_A \ln P\,dx'dy'$$
$$=\lim_{\varepsilon\to 0}\frac{1}{2}\int_{A-A_\varepsilon}\nabla_s'\bullet\left[\left(P\ln P-\frac{P}{2}\right)P\right]dx'dy' \quad (30)$$
$$+\lim_{\varepsilon\to 0}\int_{A_\varepsilon}\ln P\,dx'dy'$$

where A_ϵ is a small circular region of radius ϵ enclosing the observation point included to make the integrand continuously differentiable. For more information, see [21]. A divergence theorem can be applied to (30) to express the surface integral in terms of a flux integral around the boundary enclosing the area A. Following the result derived in [21], (30) is evaluated as

$$I_{v2,in}(u,v)=\frac{1}{2}\sum_{i=1}^{4}\vec{P}_i^0\bullet\hat{u}_i\left[l_i^+\ln P_i^+-l_i^-\ln P_i^-\right.$$
$$\left.+P_i^0\left(\tan^{-1}\left(\frac{l_i^+}{P_i^0}\right)-\tan^{-1}\left(\frac{l_i^-}{P_i^0}\right)\right)-\frac{3}{2}\left(l_i^+-l_i^-\right)\right] \quad (31)$$

where $\vec{P}_i^0=P_i^0\hat{P}_i^0$, $\hat{P}=(\vec{\rho}'-\vec{\rho})/P$, and $\hat{u}$ is the outward normal vector (ensure $\hat{z}\cdot\left(\hat{u}_i\times\hat{l}_i\right)>0$, else set $\hat{u}_i=-\hat{u}_i$).

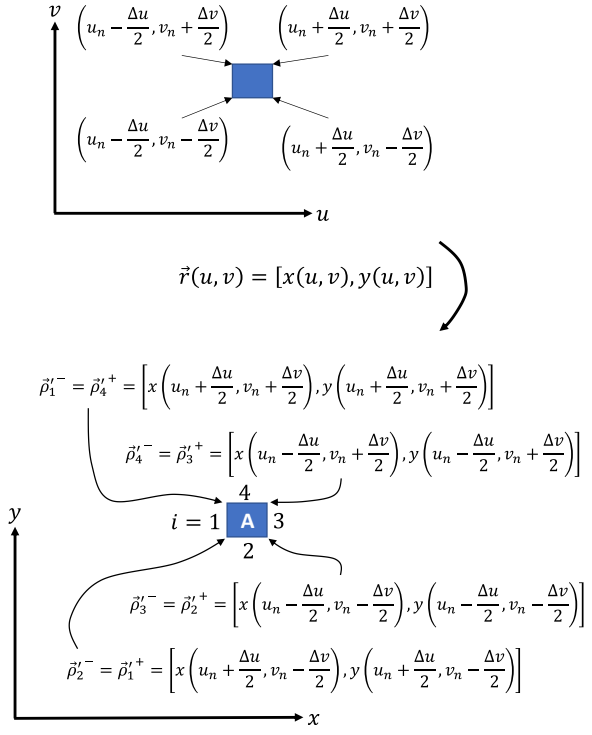

Fig. 17. Mapping of a quadrilateral patch in uv-space to its corresponding quadrilateral patch A in the xy-space.

Note, the mapping in (4) negates the signed area (Jacobian determinant is negative), and thus, going clockwise around the perimeter of the quadrilateral patch in the uv-space maps to a counterclockwise path around the perimeter of A in the native xy-space (see Fig. 17). Index i denotes one of the four sides of the quadrilateral patch in R bounding the surface area A, and thus each side i is represented by the geometry in Fig. 16.

Note, although the quadrilateral patch in the uv-space is rectangular (is constructed from straight line segments), its image under the mapping $\vec{r}$ may have curved bounding line segments. However, if the discretization is fine enough, the perimeter of A can be approximated as constructed from straight line segments, and the results of Fig. 16 will hold. With this result, (28) is found as

$$I_v = \frac{\eta_0 k_0}{4}\int_{v=v_m-\Delta v/2}^{v=v_m+\Delta v/2}\int_{u=u_m-\Delta u/2}^{u=u_m+\Delta u/2}\int_{v'=v_n-\Delta v/2}^{v'=v_n+\Delta v/2}\int_{u'=u_n-\Delta u/2}^{u'=u_n+\Delta u/2}\left[1-j\frac{2}{\pi}\ln\left(\frac{\gamma}{2}k_0\right)\right]$$
$$\times\left|\begin{matrix}\partial x/\partial u' & \partial y/\partial u'\\ \partial x/\partial v' & \partial y/\partial v'\end{matrix}\right|\left|\begin{matrix}\partial x/\partial u & \partial y/\partial u\\ \partial x/\partial v & \partial y/\partial v\end{matrix}\right| du'dv'dudv$$
$$-j\frac{\eta_0 k_0}{2\pi}\int_{v=v_m-\Delta v/2}^{v=v_m+\Delta v/2}\int_{u=u_m-\Delta u/2}^{u=u_m+\Delta u/2} I_{v2,in}(u,v)\left|\begin{matrix}\partial x/\partial u & \partial y/\partial u\\ \partial x/\partial v & \partial y/\partial v\end{matrix}\right| dudv \quad (32)$$

This completes the singular term evaluations.

ACKNOWLEDGMENT

The author would like to acknowledge contributions by Professor Anthony Grbic and Dr. Luke Szymanski from the University of Michigan on previous related works. This work was supported by the National Science Foundation grant 2247287.

REFERENCES

[1] A. Michaels and E. Yablonovitch, "Inverse design of near unity efficiency perfectly vertical grating couplers," *Opt Express*, vol. 26, no. 4, 2018.

[2] K. Achouri and C. Caloz, "Space-Wave Routing via Surface Waves Using a Metasurface System," *Sci Rep*, vol. 8, no. 1, p. 7549, Dec. 2018.

[3] S. N. Tcvetkova, D.-H. Kwon, A. Díaz-Rubio, and S. A. Tretyakov, "Near-perfect conversion of a propagating plane wave into a surface wave using metasurfaces," *Phys Rev B*, vol. 97, no. 11, p. 115447, Mar. 2018.

[4] H. Lee and D.-H. Kwon, "Large and efficient unidirectional plane-wave–surface-wave metasurface couplers based on modulated reactance surfaces," *Phys Rev B*, vol. 103, no. 16, p. 165142, Apr. 2021.

[5] A. Foroozesh, R. Paknys, D. R. Jackson, and J.-J. Laurin, "Beam Focusing Using Backward-Radiating Waves on Conformal Leaky-Wave Antennas Based on a Metal Strip Grating," *IEEE Trans Antennas Propag*, vol. 63, no. 11, pp. 4667–4677, Nov. 2015.

[6] H. Lee and D.-H. Kwon, "Conformal Metasurfaces on a Grounded Dielectric Substrate for Leaky-Wave Antennas," in *2022 IEEE International Symposium on Antennas and Propagation and USNC-URSI Radio Science Meeting (AP-S/URSI)*, 2022, pp. 451–452.

[7] H. Lee and D.-H. Kwon, "Microwave Metasurface Cloaking for Freestanding Objects," *Phys Rev Appl*, vol. 17, no. 5, p. 054012, May 2022.

[8] J. Budhu and A. Grbic, "Recent advances in bianisotropic boundary conditions: theory, capabilities, realizations, and applications," *Nanophotonics*, vol. 10, no. 16, pp. 4075–4112, Nov. 2021.

[9] J. Budhu and A. Grbic, "Perfectly Reflecting Metasurface Reflectarrays: Mutual Coupling Modeling Between Unique Elements Through Homogenization," *IEEE Trans Antennas Propag*, vol. 69, no. 1, pp. 122–134, Jan. 2021.

[10] J. Budhu, E. Michielssen, and A. Grbic, "The Design of Dual Band Stacked Metasurfaces Using Integral Equations," *IEEE Trans Antennas Propag*, pp. 1–1, Feb. 2022.

[11] J. Budhu, L. Szymanski, and A. Grbic, "Design of Planar and Conformal, Passive, Lossless Metasurfaces That Beamform," *IEEE Journal of Microwaves*, vol. 2, no. 3, pp. 401–418, Jul. 2022.

[12] W. C. Gibson, *The Method of Moments in Electromagnetics*, 3rd ed. Boca Raton: CRC Press, 2021.

[13] O. Miller, "Photonic Design: From Fundamental Solar Cell Physics to Computational Inverse Design," University of California Berkeley, Berkeley, CA, 2012.

[14] L. Szymanski, G. Gok, and A. Grbic, "Inverse Design of Multi-Input Multi-Output 2-D Metastructured Devices," *IEEE Trans Antennas Propag*, vol. 70, no. 5, pp. 3495–3505, May 2022.

[15] J. Budhu and A. Grbic, "Aperiodic Metasurface Synthesis Techniques and Designs," in *Metamaterials-by-Design: Theory, Technologies, and Vision*, A. Alu, N. Engheta, A. Massa, and G. Oliveri, Eds. Bellingham, WA: SPIE Photonic Materials and Applications Series, 2023.

[16] Y. Ra'di, D. L. Sounas, A. Alù, and S. A. Tretyakov, "Parity-time-symmetric teleportation," *Phys Rev B*, vol. 93, no. 23, p. 235427, Jun. 2016.

[17] A. Epstein and G. v. Eleftheriades, "Synthesis of Passive Lossless Metasurfaces Using Auxiliary Fields for Reflectionless Beam Splitting and Perfect Reflection," *Phys Rev Lett*, vol. 117, no. 25, p. 256103, Dec. 2016.

[18] A. Yariv and P. Yeh, *Optical Waves in Crystals. Propagation and Control of Laser Radiation*. New York: John Wiley & Sons, 1984.

[19] J. Budhu, "MATLAB DESIGN CODES AND COMSOL MULTIPHYSICS SIMULATION FILES TO ACCOMPANY NEAR-PERFECT SPACE-WAVE TO SURFACE-WAVE COUPLER ENABLED CONFORMAL SPACE WAVE TRANSPORTING METASURFACES," *IEEE Dataport, https://dx.doi.org/10.21227/bb0x-7j71*, Nov. 2023.

[20] J. Budhu, N. Ventresca, and A. Grbic, "Unit Cell Design for Aperiodic Metasurfaces," *IEEE Trans*

Antennas Propag, vol. 71, no. 9, pp. 7387–7394, Sep. 2023.

[21] D. R. Wilton, D. R. Wilton, S. M. Rao, S. M. Rao, A. W. Glisson, D. H. Schaubert, D. H. Schaubert, O. M. Al-Bundak, C. M. Butler, and C. M. Butler, "Potential Integrals for Uniform and Linear Source Distributions on Polygonal and Polyhedral Domains," *IEEE Trans Antennas Propag*, vol. 32, no. 3, 1984.

Jordan Budhu (Member, IEEE) Jordan Budhu received his M.S. degree in electrical engineering from the California State University, Northridge, California, USA, in 2010, and the Ph.D. degree in electrical engineering from the University of California, Los Angeles, California, USA, in 2018.

He was hired as an Assistant Professor with Virginia Tech, Blacksburg, VA, USA, in 2022, where he is currently the Steven O. Lane Junior Faculty Fellow of electrical and computer engineering with the Bradley Department of Electrical and Computer Engineering. He was a Postdoctoral Research Fellow in the Radiation Laboratory and a Lecturer in the Department of Electrical Engineering and Computer Science at the University of Michigan, Ann Arbor, Michigan, USA from 2019 to 2022. In 2011 and 2012, he was a Graduate Student Intern at the NASA Jet Propulsion Laboratory. In 2017, he was named a Teaching Fellow at the University of California, Los Angeles. His research interests are in metamaterials and metasurfaces, computational electromagnetics algorithms for metamaterial and metasurface design, conformal beamforming antennas, nanophotonics and metamaterials for the infrared, 3D printed inhomogeneous lens design, CubeSat antennas, reflectarray antennas, and antenna theory.

Dr. Budhu's awards and honors include the 2010 Eugene Cota Robles Fellowship from UCLA, the 2012 Best Poster award at the IEEE Coastal Los Angeles Class-Tech Annual Meeting, the 2018 UCLA Henry Samueli School of Engineering and Applied Science Excellence in Teaching Award, the first-place award for the 2019 USNC-URSI Ernst K. Smith Student Paper Competition at the 2019 Boulder National Radio Science Meeting, and the Steven O. Lane Junior Faculty Fellowship of Electrical and Computer Engineering in the Bradley Department of Electrical & Computer Engineering at Virginia Tech.